Acc. Chem. Res. **2002,** *35,* 1054−1062

Structural Characterization of Atomically Regulated Nanocrystals Formed within Single-Walled Carbon Nanotubes Using Electron Microscopy

JEREMY SLOAN,*,†,‡ ANGUS I. KIRKLAND,*,§ JOHN L. HUTCHISON,‡ AND MALCOLM L. H. GREEN†

Inorganic Chemistry Laboratory, University of Oxford, South Parks Road, Oxford, OX1 3QR, U.K., Department of Materials, University of Oxford, Parks Road, Oxford, OX1 3PH, U.K., and Department of Materials Science and Metallurgy, University of Cambridge, Pembroke Street, Cambridge CB2 3QZ, U.K.

Received March 4, 2002

ABSTRACT

The structural chemistry of nanoscale materials encapsulated within single-walled carbon nanotubes (SWNTs) is reviewed. SWNTs form atomically thin channels within a restricted diameter range, and their internal van der Waals surfaces regulate the growth behavior of encapsulated crystals in a precise fashion, leading to atomically regulated growth. The structural properties of these systems are largely dictated by the structural chemistry of the bulk material, although significant deviations from bulk structures are often observed, with lower surface coordinations and substantial lattice distortions.

1. Introduction

In 1959,[1] Richard Feynman asked, "What could we do with layered structures with just the right layers? What would the properties of materials be if we could really arrange the atoms the way we want them?" He also noted that, "They would be very interesting to investigate theoretically...I can hardly doubt that when we have some control of the arrangement of things on a small scale we will get... [a] greater range of possible properties that substances can have, and of different things that we can do." Substantial advances in fabrication and related technologies since 1959 have made it possible to manipulate matter on an atomic scale,[2−9] and this Account outlines of one of the most promising approaches to the production of discrete atomically regulated structures by encapsulation within single-walled carbon nanotubes (SWNTs).

SWNTs are formed from rolled sheets of sp^2 graphene carbon[10,11] which form well-defined cylindrical cavities with a strictly limited diameter range (1−2 nm)[12,13] when synthesized in a controlled fashion. Depending on the orientation of the six-membered carbon rings with respect to the nanotube axis, either achiral (zigzag or armchair, Figure 1a,b) or chiral (Figure 1c) nanotubes can be constructed.[14] Encapsulated guest materials can be introduced into these cavities by a number of methods,[15,16] and in particular capillary filling of SWNTs with molten salts[17,18] allows the crystallization of atomically regulated structures with reduced, modified, or entirely novel coordinations compared to the bulk.[19,20]

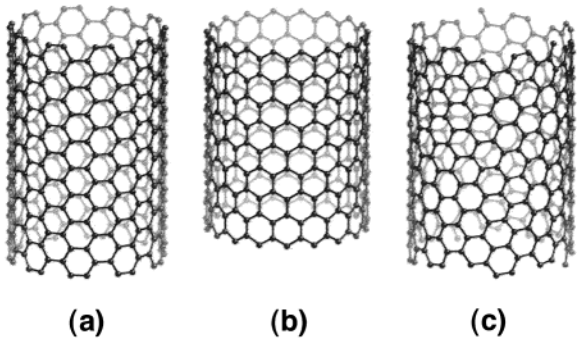

FIGURE 1. Schematic representation of the structures of (a) armchair, (b) zigzag, and (c) chiral SWNTs of similar diameters.

The accurate, quantitative structural characterization of these nanocomposites presents a number of challenges. To fully understand the consequences of nanoscale encapsulation, it is necessary to acquire both structural and chemical information at high spatial resolution and

* To whom correspondence should be addressed. J.S.: E-mail jeremy.sloan@chem.ox.ac.uk, tel. +44-1865-272645, fax +44-1865-272690. A.I.K.: E-mail aik10@cam.ac.uk, tel. +44-1223-334568, fax +44-1223-334567.

† Inorganic Chemistry Laboratory, University of Oxford.

‡ Department of Materials, University of Oxford.

§ Department of Materials Science and Metallurgy, University of Cambridge.

Jeremy Sloan obtained his B.Sc. in chemistry from the University of Hull in 1982, his M.Sc. in 1989 from the State University of New York at Binghamton, and his Ph.D in solid-state chemistry in 1995 from the University of Wales, Cardiff, under the supervision of Professor Richard Tilley FRSC. He joined the Inorganic Chemistry Laboratory at Oxford in 1995 as a postdoctoral research assistant to Professor Malcolm Green FRS. In 2000 he was awarded a Royal Society University Research Fellowship. He is a member of Wolfson College.

Angus Kirkland graduated with a B.A. from the University of Cambridge in 1983 and was awarded his M.A. and Ph.D. in electron microscopy from the University of Cambridge in 1989. He then spent two years as an EPSRC research associate in the Department of Chemistry in Cambridge. In 1991 he was awarded the Ramsay Memorial Research Fellowship, followed by appointment as an Isaac Newton Trust research associate in the Departments of Materials Science and Chemistry at Cambridge in 1994 and to his current post as Senior Research Fellow in 1997. He was elected a fellow of Fitzwilliam College, Cambridge, in 1992.

John Hutchison obtained his B.Sc. in chemistry from Glasgow University in 1967, followed by his Ph.D. in 1970. From 1970 to 1975 he was a postdoctoral research fellow in the Inorganic Chemistry Laboratory in Oxford and subsequently took up an appointment as a research associate at the University of Wales, Aberystwyth. In 1979 he returned to Oxford and has successively held appointments as an SERC Advanced Fellow, Senior Research Fellow, and Research Lecturer. In 1999 he was promoted to Reader in Materials. He was awarded the Royal Microscopical Society's Glauert Medal in 1974 and is currently the Society's Vice President and International Secretary.

Malcolm Green was awarded his B.Sc. from the University of London in 1956 and his Ph.D. from Imperial College of Science and Technology, London, in 1959. From 1960 to 63 he was an Assistant Lecturer in the Inorganic Chemistry Department at Cambridge. He moved to Oxford in 1963 on appointment as a Fellow in Inorganic Chemistry at Balliol College and was appointed University Lecturer in 1965. He was promoted to Professor of Inorganic Chemistry and head of the Inorganic Chemistry Laboratory in Oxford in 1988. He is a Fellow of the Royal Society, a Fellow of St Catherines College, Oxford, and an Emeritus Fellow of Balliol College, Oxford.

10.1021/ar010169x CCC: $22.00
Published on Web 09/24/2002

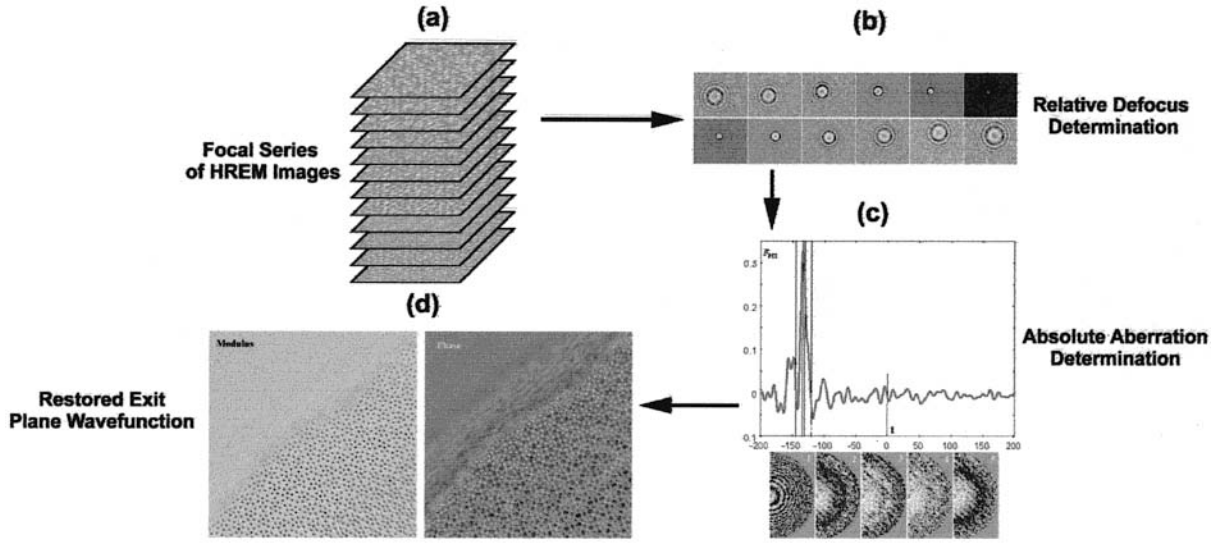

FIGURE 2. Schematic illustration of the steps involved in data acquisition and analysis for indirect wave function restoration from conventional HREM images. (a) Collection of a focal series of conventional HREM images. (b) Relative defocus determination between pairs of images by maximizing the peak height of the phase correlation function between them for varying defocus values. (c) Absolute aberration determination by maximizing the integrated intensity in the phase contrast index function as a function of defocus. (d) Exit plane wave function restoration using the aberrations determined in (c).

sensitivity. Conventional "broad beam" diffraction or spectroscopy is often unsuitable due to macroscopic sample inhomogeneities, and hence the development of advanced transmission electron microscopy techniques is proving to be essential[21,22] due to the availability of both structure images at atomic resolution and intense subnanometer probes for chemical analysis.

In this Account, we outline a combinatorial approach to the application of such techniques in the study of atomically regulated structures formed within SWNTs, illustrated with examples from a range of inorganic systems.

2. Electron Microscopy

Transmission electron microscopy (TEM) is an invaluable tool in the determination of the structure and structural chemistry of nanocrystalline materials. Modern instrumentation,[23,24] using field emission electron sources and operating at intermediate (200−300 kV) voltages, provides imaging at close to atomic resolution,[25] together with subnanometer diameter bright probes which can be used to collect electron energy loss spectra (EELS)[26] and to map characteristic X-ray emission spectra (EDX).[27]

To further increase the usefulness of this technique, a number of alternative approaches to image reconstruction or restoration[28−35] have been developed and applied to high-resolution electron microscope (HREM) images. These provide an *indirect* route to improved spatial resolution and simultaneously dramatically improve the level to which data can be interpreted in a quantitative fashion. Such methods recover both the phase and modulus of the exit surface wave function resulting from the interaction of the electron beam with the specimen, with full correction of all lens aberrations rather than the aberrated (uncorrected) intensity available directly in a single conventional HREM image. They also improve the signal-to-noise ratio of the resultant structural data via averaging over a large dataset.

The simplest and most widely applied experimental approach to restoration requires the collection of a set of (typically 20 or more) conventional axial HREM images recorded at different defocus levels.[28−31] In such a dataset, the differently aberrated (defocused) images provide independent information, thus overdetermining the specimen exit plane wave function, which can be recovered easily for thin specimens where imaging process are complicated but essentially linear.[28,29,34]

Until recently, this approach has been limited by three factors: (i) nonlinear components of the image intensity which increase with specimen thickness, (ii) intensities arising from inelastically scattered electrons, and (iii) the range of directions and energies present in the electron beam which reduce the spatial and temporal coherence, hence limiting the ultimately achievable resolution. However, significant technical developments have greatly changed this situation. In the first instance, efficient computational approaches which account for the nonlinear imaging interactions have been developed.[31] In parallel, the development of energy-filtered imaging systems[36,37] has enabled the intensity from electrons scattered inelastically by mechanisms other than phonon scattering to be eliminated from individual HREM images. Finally, field-emission electron sources are now commercially available,[38,39] offering improved temporal and spatial coherence, giving images containing higher spatial frequencies, so that focal series reconstruction achieves higher resolution. In addition to the above, the increased availability of fully characterized CCD cameras for digital image recording[40,41] has made it easier to record the sets of images needed for reconstruction in a quantitative and reliable manner.

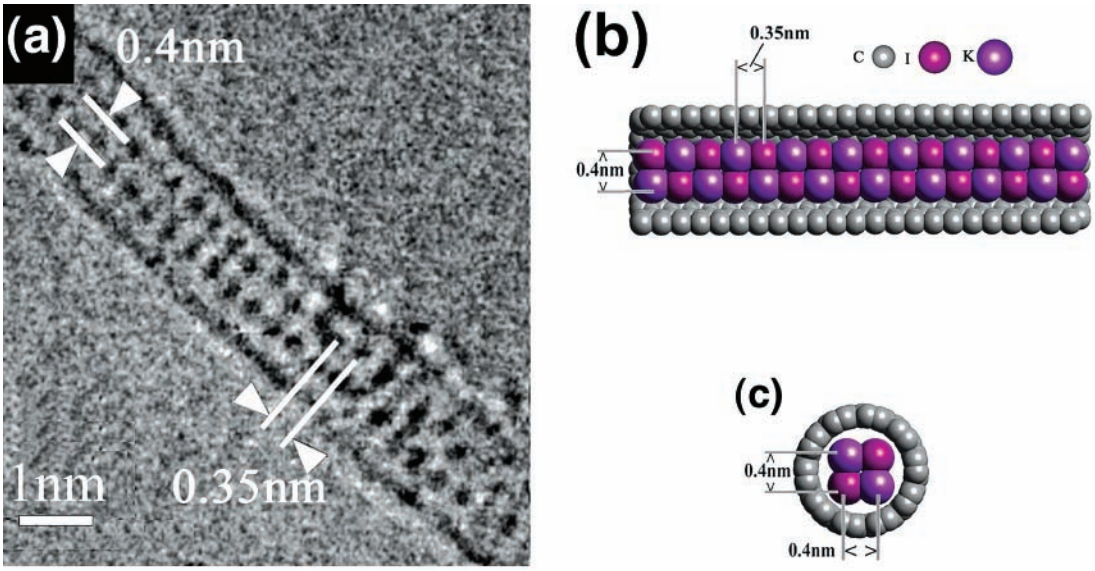

FIGURE 3. (a) Conventional HREM image recorded at the Scherzer defocus of a 2 × 2 KI crystal formed within a 1.4-nm-diameter SWNT in a ⟨100⟩ projection. (b,c) Respectively side-on and end-on structural representations of the 2 × 2 KI crystal within a SWNT, showing measured lattice spacings.

In practice, the recovery of the exit surface wave function initially involves the determination of the aberrations present in each individual image using one of several established methods.[21,22,42] Subsequently, the complex wave function itself is recovered from a summation of these images with the application of appropriate restoring filters determined from the individual imaging conditions. In the case of SWNTs, the modulus of the exit surface wave function is generally extremely weak due to the weak electron scattering by very thin crystals, and hence we have largely used the phase to provide structural information. Schematically, this process is summarized in Figure 2.[42] The benefits of this approach are to allow structural inferences about the specimen to be made by direct comparison of predicted and observed wave functions, with only two real unknowns, the specimen structure and thickness. In the case of materials encapsulated within SWNTs, the latter can often be inferred from the cylindrical symmetry of the SWNT. Using this indirect approach, we have been able to directly deduce the detailed atomic arrangement of a variety of nanocrystalline encapsulated materials, examples of which are detailed in subsequent sections.

3. Metal Halide-Filled Nanotubes

Metal halides form the most comprehensive series of currently characterized filling materials, with many examples within several distinct structural families known.[43−46] For bulk binary halides, a simple classification scheme according to stoichiometry, bulk structure type, and coordination[43] has been used as a guide for filling SWNTs.[44−46] The general effect of confining these materials into SWNTs is to form structures that are *specified* by both the bulk structure of the incorporated halide and the confining surface of the encapsulating nanotube. In certain cases, however, the former does not apply, and entirely new structures can be formed. In the remaining cases, structures may be distorted or otherwise modified by encapsulation.

For simple packed halides, confinement leads to the formation of "Feynman crystals",[1] in which the number of atomic layers is precisely regulated by the confining surface of the SWNT. The first example reported is a 2 × 2 KI crystal formed within a 1.4-nm-diameter SWNT (Figure 3).[19] Conventional HREM images (Figure 3a) show an ordered array of pairs of identical dark spots along the SWNT capillary, with each of these representing an individual I−K or K−I column viewed in projection along a ⟨100⟩ direction (Figure 3b,c). This results in all the ions undergoing a *total reduction in coordination*, from 6:6, as found in the bulk, to 4:4. Lattice distortions are also observed in these crystals, with a {200} spacing along the tube axis of ∼0.35 nm, similar to the {200} spacing of bulk KI, but expanded to ∼0.4 nm across the capillary.[19]

We have also characterized a 3 × 3 KI crystal in a larger diameter (1.6 nm) SWNT (Figure 4).[20] In this example, images were recorded along the KI cell diagonal, which in principle should allow the visualization of both the K^+ and I^- sublattices as pure element columns. However, it is not possible to observe the weaker scattering K^+ sublattice via conventional HRTEM, although the strongly scattering I^- sublattice is revealed as a series of dark spots along the tube axis (Figure 4a). Using indirect restoration, we have restored the exit plane wave function (Figure 4b) of this specimen at close to the information limit (0.1 nm) of our 300 kV FEGTEM. The additional information present in the phase of the restoration has made it possible to image the K^+ atom columns in addition to the more strongly scattering I^- atom columns. From this restored phase, direct measurements of column positions after averaging along the tube axis (Figure 4c) have enabled us to accurately determine individual column displacements within the incorporated 3 × 3 crystal, leading to a more detailed structural model (Figures 4d)

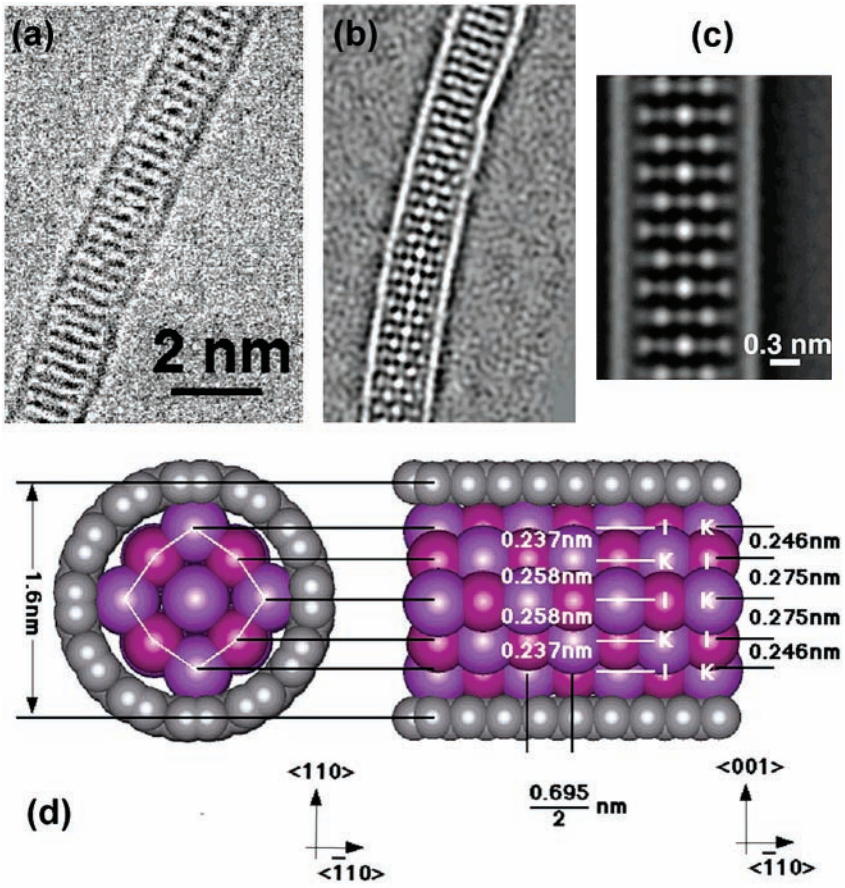

FIGURE 4. (a) Conventional HREM image recorded at the Scherzer defocus of a 3 × 3 KI crystal formed within a 1.6-nm-diameter SWNT in a ⟨110⟩ projection. (b) Reconstructed phase of the same crystal as in (a). Note that the contrast in this image is reversed so that regions of high electron density appear bright and those of low electron density appear dark. (c) Enlargement of a region from (b) after averaging along he tube axis. (d) Structural model derived from (b).

of the composite which indicates an unexpected anisotropic distortion of the KI lattice.[20]

The 3 × 3 crystal shows three separate coordinations of 6:6, 5:5, and 4:4 exhibited by the center, face, and corner ....I−K−I−K.... rows, respectively, of the 3 × 3 crystal along the SWNT axis.[20] The I^- atoms located along ⟨110⟩ show a slight inward compression relative to their positions in the bulk structure, and the K^+ atoms located along the same cell diagonal exhibit a small expansion, as do the K^+ and I^- atoms located along the shorter ⟨100⟩ directions. This distortion is thought to be due to the small compressive effect of the larger I^- ions (i.e., $I^-_{IV} \approx 0.22$ nm vs $K^+_{IV} \approx 0.13$ nm) by the van der Waals surface of the SWNT.

Wilson and Madden have modeled the crystal growth behavior of KI in variable-diameter open-ended SWNTs using molecular dynamics simulations.[47] Their time-resolved and minimum energy simulations predict filling with *thermodynamically ordered* arrays of 2 × 2 KI crystals, starting from an open SWNT immersed in molten KI, and also predict lattice distortions consistent with those observed experimentally.[19] In particular, for the case of the 2 × 2 KI crystal, the correct aspect ratio of the observed lattice distortion is reproduced,[19] while a 3 × 3 KI crystal encased in a 1.6-nm-diameter SWNT shows differential displacements for halide atoms disposed along the longest diagonal versus facial atoms disposed along the shorter ⟨100⟩ direction.[20]

Ternary halides can also be incorporated into SWNTs using the melting properties of the pseudoternary AgCl−AgI phase diagram, allowing, for example, the eutectic AgCl−AgI composition to be incorporated into SWNTs[17] which, as it contains one strongly scattering halogen (I, $Z = 53$ vs Cl, $Z = 17$), facilitates preferential imaging via conventional HREM.

HREM observation of this composite reveals that it contains a mixture of filling materials, approximately 70% of which are crystalline while ca. 30% are disordered. The crystalline filling consists of two components: (i) a metallic Ag filling presumed to originate from dissociation of the halide mixture and (ii) a crystalline $AgCl_{1-x}I_x$ filling. The latter is metastable, as the eutectic composition should be polycrystalline in the solid state. Figure 5a shows a ca. 2-nm-diameter SWNT filled with fcc Ag metal (with ⟨010⟩ parallel to the SWNT axis and ⟨001⟩ parallel to the electron beam), with a lattice spacing orthogonal to the axis of ca. 0.21 nm (corresponding to d_{020} for Ag). In this image, the walls of the SWNT are visible as vertical lines on either side of the encapsulated nanocrystal (Figure 5c). Figure 5b shows an image of the metastable crystalline halide with an average periodicity of ca. 0.4 nm along the

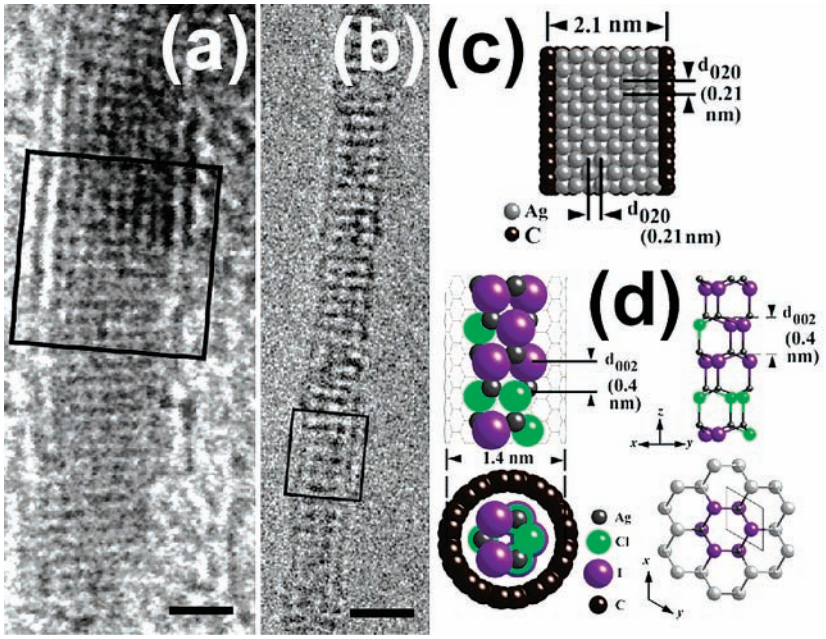

FIGURE 5. (a) HREM image of Ag crystal within a SWNT (scale bar = 1 nm). (b) HREM image of encapsulated crystalline $AgCl_{1-x}I_x$ (scale bar = 2 nm). (c) Structure model of encapsulated Ag nanocrystal. (d) Side-on (top) and end-on (bottom) representations of 1D wurzite tunnel structure together with a staggered ball-and-stick representation (top) and schematic showing derivation of the tunnel structure from the ⟨001⟩ direction of wurzite AgI.

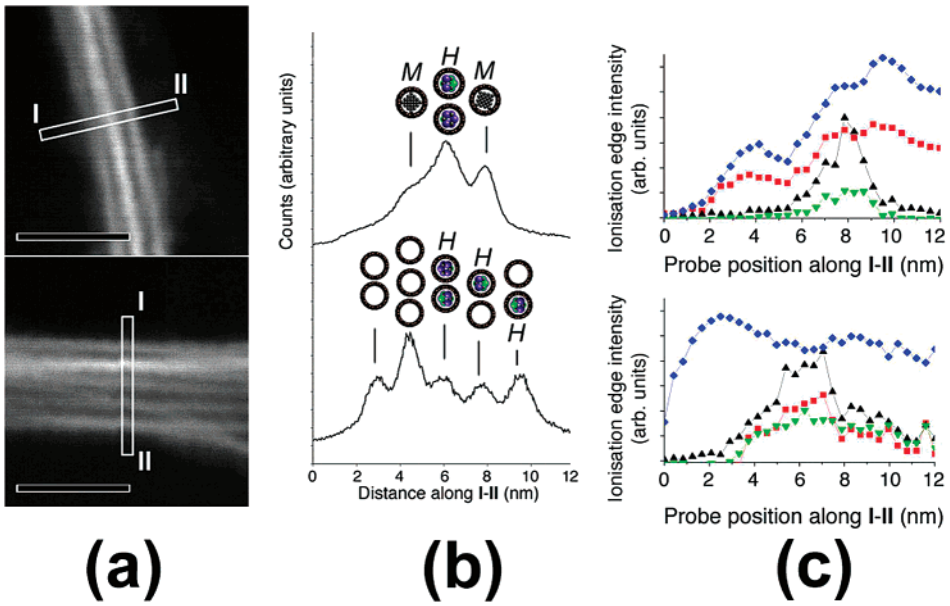

FIGURE 6. (a) HAADF images. (b) Contrast profiles along the indicated line I−II and filling configurations. Key: *H* = halide-filled SWNT; *M* = metal-filled SWNT. (c) Integrated EELS profiles obtained from (top) two bundles containing ca. four SWNTs and (bottom) a bundle containing eight or nine SWNTs (all scale bars = 10 nm).

SWNT axis formed within a 1.4-nm-diameter SWNT. The microstructure of the encapsulated material is imaged as a staggered array of distorted dark spots that suggest a 1D "tunnel" structure derived from wurzite AgI (Figure 5d). In the corresponding model, each dark spot in the lattice image corresponds to slightly staggered columns of either X−Ag−X or Ag−X−Ag, and the contrast variations in the spots can be attributed to a random distribution of weaker scattering Cl^- and stronger scattering I^- over the X^- sites (Figure 5d).

To obtain further compositional information, spatially resolved EELS has also been used to probe the local composition of the encapsulated material. Figure 6a shows typical high-angle annular dark field (HAADF) images obtained from SWNT bundles recorded using a dedicated scanning transmission electron microscope (STEM) together with compositional models and EEL spectra obtained at different probe positions. In this sample, the I and Cl edges were always observed together whenever halide was detected, indicating that the AgCl−AgI mixture melts congruently into the SWNTs. Additionally, the determined Cl:I ratios varied from ca. 10:1 to 1:10, thus supporting the previous hypothesis that local concentrations of Cl and I vary on an unsystematic basis. Additional

EELS line scans confirm the formation of elemental Ag in some SWNTs, corresponding to those in which electron beam-induced reduction has occurred. Overall, these results provide clear evidence for the formation of an encapsulated ternary crystalline halide phase within SWNTs.

4. Metal Oxide-Filled Nanotubes

A second important class of encapsulated materials is inorganic oxides, albeit one from which fewer examples have been fully characterized, in part due to a lack of availability of relatively low melting point precursors suitable for encapsulation via capillary filling. In this section, one such example is described, together with an outline of the detailed characterization of the *encapsulating* nanotube chirality.

Figure 7a shows the restored phase of a 1.5-nm-diameter SWNT containing an encapsulated single crystal of Sb_2O_3. It is clear that the right wall of the SWNT displays fringes with a spacing of 2.24 Å, whereas the contrast variations on the left wall are random, as confirmed by 1D power spectra obtained from single-pixel line traces along the tube walls (Figure 7b). The restoration process allows us to directly determine the inclination of the nanotube with respect to the image plane from the defocus levels calculated for individual subregions. This information, together with the presence of asymmetric fringe contrast with a spacing of 0.224 nm, enables us to rationalize the observed contrast by exhaustive comparison of the restored wave function with those simulated for 1.5-nm-diameter tubes with a range of different chiral angles and orientations close to those observed experimentally. These simulations indicate that in achiral *zigzag* tubes this spacing is observable in both tube walls but is entirely absent in armchair tubes,[48] where the spacing between adjacent carbon atom rows is less than the resolution of the restoration. If the tube axis is tilted away from the image plane, the contrast remains equal on both walls for achiral tubes, but the fringes observed for the zigzag conformation become increasingly blurred at higher tilts due to a staggering of the carbon atoms in projection. Chiral tubes, however, display strong asymmetric contrast on one tube wall for certain inclinations of the tube from the image plane,[48] which corresponds closely to that observed experimentally. Additional information is provided by the 2D power spectrum of the restored wave, which shows reflections that are incommensurate with those of the encapsulated Sb_2O_3 with a component perpendicular to the tube axis corresponding to the spacing observed in the right tube wall. Overall, therefore, using this methodology, we have been able to assign both the chiral vector of the SWNT and its sense.[48]

The restored phase (Figure 7a) shows contrast due to the filling material in the SWNT over the entire field of view. However, only within the lower region of the tube is the crystalline Sb_2O_3 suitably oriented for detailed structural characterization. Figure 8a shows an enlargement of this subregion, with frequencies greater than those of the highest crystal reflections filtered to reduce unnecessary noise. The uninterpretable crystalline contrast in the remainder of the tube arises from movement and rotation of the tube during data acquisition and from misorientation of the filling in these tube regions. Within the lower region, the filling can be identified as a Sb_2O_3 single crystal in the valentinite form (i.e., the high-pressure

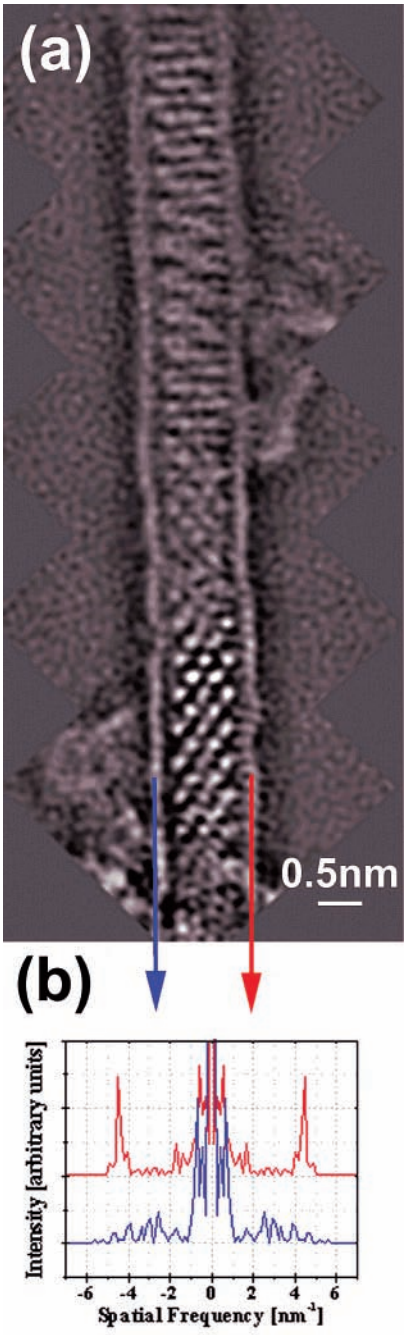

FIGURE 7. (a) Restored phase of a Sb_2O_3-filled SWNT. The image is composed of six individually restored overlapping subregions. The lower part shows the crystalline Sb_2O_3 clearly resolved along a projection close to ⟨1 0 −1⟩ together with regular fringe contrast in the right-hand wall of the tube. (b) Power spectrum taken from 1D linescans along the tube walls indicated by arrows in (a). The spectrum for the right wall (red) shows a strong peak corresponding to a spacing of 0.224 nm which is absent in that for the left wall (blue). This asymmetric fringe contrast indicates that the tube is chiral and inclined to the image plane.

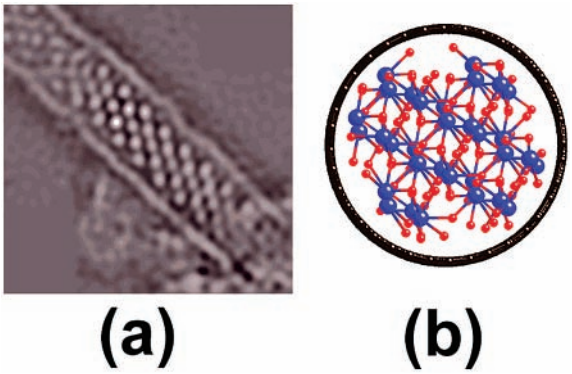

FIGURE 8. (a) Noise-filtered phase detail taken from Figure 7a. (b) Ball and stick representation of the valentinite Sb_2O_3 crystal fraction viewed along the SWNT axis.

form of Sb_2O_3[49] as opposed to its cubic senarmonite form consisting of molecular units of Sb_4O_6[50]). In the bulk, valentinite consists of infinite chains of Sb_2O_3 units running parallel to ⟨001⟩, where each antimony atom is coordinated by three oxygen atoms, each bridging two independent antimony atoms. In the encapsulated Sb_2O_3 crystal, we have determined that the ⟨4 −1 2⟩ direction of this fragment is aligned with the tube axis and that the tube is inclined at an angle of ca. 15° from the image plane. The white spots in the reconstructed phase correspond to the positions of the antimony sublattice only, as due to the weak scattering of oxygen and a limited resolution (of ca. 0.14 nm) in the restoration, the oxygen sublattice could not be resolved, as confirmed by image simulations.[48] This analysis suggests that the structure of the encapsulated Sb_2O_3 crystal can be described as a repeated sequence of a row containing three Sb atom columns followed by a row containing two Sb atom columns perpendicular to the long axis of the tube. The rows consisting of three columns show a contrast consistent with a stacking pattern of 3−2−3 antimony atoms in projection, and the rows of two columns show a contrast consistent with three antimony atoms in projection. These observations have allowed us to construct a model Sb_2O_3 crystal fraction, which has sequences of 3−2−3 and 3−3 layers with an 4-fold repeat period along the ⟨4 −1 2⟩ direction, which gives simulated contrast that closely matches that observed experimentally. Within the experimental nanocrystal, there is also evidence for local structural irregularity, with some two-column rows showing ca. 30% greater intensity at the atom sites compared with other rows of this type. This suggests a possible antimony stacking pattern of 4−4 in these particular rows; in a similar fashion, the center row of the crystal (parallel to the tube axis) also contains certain columns of three antimony atoms rather than the usual two antimony atoms. Overall, these observations have allowed us to construct the final structural model for the encapsulated nanocrystal shown in Figure 8b. In addition to the local inhomogeneities described above, significant lattice distortions were also observed in the encapsulated material. In comparison to the bulk structure of valentinite, the encapsulated crystal shows a longitudinal contraction of ∼13% along the ⟨4 −1 2⟩ axis, with an average spacing of ∼0.552 nm between the two-column rows and the three-column rows compared to the average bulk spacing of ∼0.638 nm.

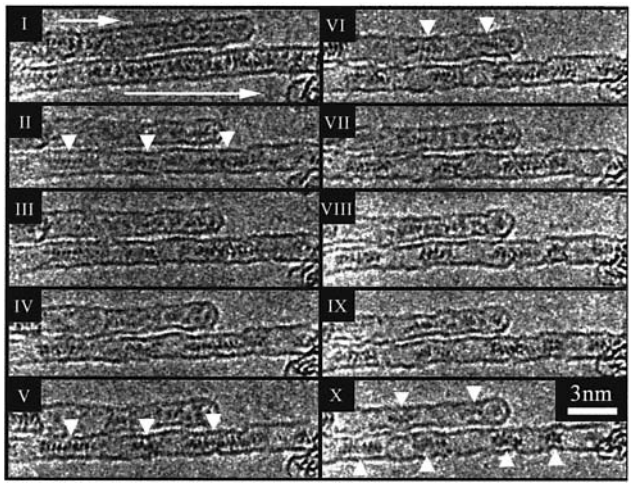

FIGURE 9. Sequence of HREM images I−X obtained at ca. 20-s intervals, showing gradual clusterization of encapsulated $ZrCl_4$ induced by electron beam irradiation.

5. Direct Observation of Dynamic Events

The previous sections have given representative examples of filling materials that are sufficiently stable under electron irradiation to permit detailed structural characterization. However, a number of encapsulated materials are electron beam sensitive, undergoing complex rearrangement processes during electron exposure. This section describes one such example involving "clusterization" of $ZrCl_4$ with elimination of Cl_2, a process that can be directly followed by recording a continuous video sequence of conventional HREM images.[51]

HREM examination of this composite shows that the as-prepared SWNTs are initially filled with continuous chains of $ZrCl_4$ which exhibit a 1D chain-type halide structure in the bulk. Subsequent irradiation of this material at 300 kV with an intense electron beam causes the filling material to undergo progressive changes in morphology as it segregates to form discrete clusters. We have successfully followed a typical sequence of events over periods of up to 20 min, after which the encapsulating SWNTs denatured.

Figure 9 shows a typical sequence of 10 images taken from individual video frames obtained over a period of ∼4 min. In the initial image (I), two continuously filled SWNTs are observed, with the upper tube terminated by a cap visible on the right of the image. By image II, the filling in the bottom tube has already segregated into three ∼3- to 4-nm-long clusters, and subsequently in image V the clusters indicated with arrows undergo structural alteration to give clusters with different lengths of 3, 2, and 4 nm. In image VI, the material in the topmost tube has also segregated into a pair of clusters, and finally in image X, discrete ∼1-nm-long clusters can be seen in both nanotubes, with the number of clusters in the bottom tube having increased from three to four (cf. image V). Eventually, following long-term irradiation for a ∼10-min period,

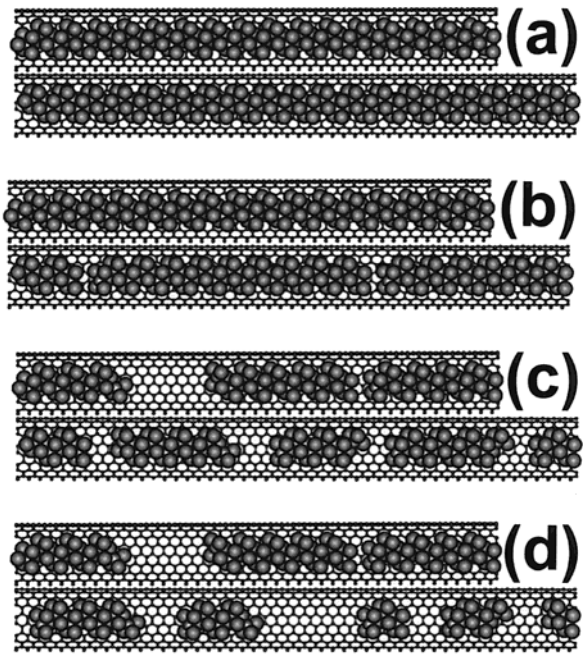

FIGURE 10. Idealized structural representation of cluster formation within a pair of SWNTs, illustrating the principal changes described in the text. (a) Continuous filling of an unbroken $ZrCl_4$ chain. (b) Partial irradiation causes breaks in this chain and elimination of chlorine occurs, resulting in the formation of reduced halide polyhedra at the chain termini. (c) Formation of smaller clusters. (d) Final formation of discrete separated clusters.

a minimum length of ~1 nm for the clusters is observed. It is important to note that during these initial transformations (i.e., before the final denaturing of the SWNTs themselves), the walls of the tubules appear to be unchanged, suggesting that no substantial chemical interaction between the carbon walls and the filling material occurs during this "clusterization" process.

The image contrast from the initial microstructure of the filling material in image I is indistinct, whereas several of the longer clusters in images II, III, and V show arrays of dark spots similar to those reported for $CdCl_2$ and other related structures.[44,53] It is therefore reasonable to suppose that $ZrCl_4$, which forms an edge-sharing "trans" octahedral chain structure in the bulk,[54] forms similar 1D chains within SWNT capillaries. During initial electron beam irradiation, these chains undergo sequential elimination of chlorine to form clusters with a stoichiometry of $ZrCl_x$, where $x < 4$. Figure 10 shows an idealized schematic representation of this cluster formation process. Initially (Figure 10a), the continuous filling of an unbroken $ZrCl_4$ chain is shown. Subsequent irradiation initially causes breaks in this chain (Figure 10b), and at the sites of these breaks, elimination of chlorine occurs, resulting in the formation of reduced halide polyhedra at the chain termini. It is assumed that the eliminated molecules of Cl_2 diffuse through side-wall defects or the end-caps of the SWNTs. During further irradiation, small clusters form (Figure 10c), followed by discrete separated clusters at a later stage (Figure 10d). This result illustrates that it is possible to follow and understand dynamic events occurring within encapsulated materials in real time using continuously recorded video sequences of HREM images. It is also interesting to speculate that if this mode of cluster formation can be reproduced for a bulk semiconductor-filled SWNT sample—for example by use of an alternative decomposition methodology—then it may be possible to produce aligned 1D quantum dot arrays within SWNTs.[55]

6. Conclusions

In this Account, we have reviewed the use of advanced electron microscopy for the detailed structural characterization of a variety of materials within SWNTs. Within these very narrow capillaries, the structures obtained often have an integral number of atomic layers in two dimensions but are effectively infinite in the third dimension. The nature of the encapsulated structures often varies from the bulk material, with evidence for reduced coordination, local inhomogeneity, and significant lattice distortions. Under specific conditions, the chirality of the encapsulating tube can also be determined from a detailed analysis of the wall contrast and an accurate estimate of the tube inclination. It is possible to modify the inserted crystals chemically either by photolytic reduction or by in situ electron beam irradiation experiments in which encapsulated halide crystals may be reduced to form either metallic nanowires or templated clusters with regulated dimensions.

The authors are indebted to a large number of collaborators who have contributed to this project, including, in Oxford, David Wright, Gareth Brown, Sam Bailey, Steffi Friedrichs, Cigang Xu, Miles Novotny, Dr. Karl Coleman, Prof. Hee-Gweon Woo, Dr. Emmanuel Flahaut, and Dr. Rafal Dunin-Borkowski, and in Cambridge, Rüdiger Meyer and Dr. Owen Saxton. We are also grateful to Dr. Mauricio Terrones (currently at IPICyT, Mexico), Dr. Stefan Nufer, and Prof. Manfred Rühle of the Max Planck Institut für Metallforschung, Stuttgart. We acknowledge financial support from the Petroleum Research Fund, administered by the ACS (Grant No. 33765-AC5), and the EPSRC (Grants Nos. GR/L59238, GR/L22324, GR/N17577, GR/R08650/01). J.S. is indebted to the Royal Society for a University Research Fellowship.

References

(1) Reproduced in: Feynman, R. P. There's Plenty of Room at the Bottom. *Eng. Sci.* **1960**, *23*, 22−36.
(2) *Quantum Dot Heterostructures*; Bimberg, D., Grundmann, M., Ledentsov, N. N., Eds.; John Wiley & Sons Ltd.: Chichester, 1999.
(3) Overney, R. M.; Meyer, E.; Frommer, J.; Brodbeck, D.; Luthi, R.; Howald, L.; Guntherodt, H.-J.; Fujihira, M.; Takano, H.; Gotoh, Y. Friction Measurements on Phase-Separated Thin Films with a Modified Atomic Force Microscope. *Nature* **1992**, *359*, 133−135.
(4) Noy, A.; Frisbie, C. D.; Rozsnyai, L. F.; Wrighton, M. S.; Lieber, C. M. Chemical Force Microscopy: Exploiting Chemically-Modified Tips To Quantify Adhesion, Friction, and Functional Group Distributions in Molecular Assemblies. *J. Am. Chem. Soc.* **1995**, *117*, 7943−7951.
(5) Sinniah, S. K.; Steel, A. B.; Miller, C. J.; Reutt-Robey, J. E. Solvent Exclusion and Chemical Contrast in Scanning Force Microscopy. *J. Am. Chem. Soc.* **1996**, *118*, 8925−8931.
(6) McKendry, R.; Theoclitou, M. E.; Rayment, T.; Abell, C. Chiral Discrimination by Chemical Force Microscopy. *Nature* **1998**, *391*, 566−568.
(7) Yau, S.-T.; Thomas, B. R.; Vekilov, P. G. Molecular Mechanisms of Crystallization and Defect Formation. *Phys. Rev. Lett.* **2000**, *85*, 353−356.
(8) Tsuchie, K.; Nagao, T.; Hasegawa, S. Structure of C_{60} layers on the Si(111)-$\sqrt{3}\times\sqrt{3}$-Ag Surface. *Phys. Rev. B* **1999**, *60*, 11131−11136.

(9) Fishlock, T. W.; Oral, A.; Egdell, R. G.; Pethica, J. B. Manipulation of Atoms Across a Surface at Room Temperature. *Nature* **2000**, *404*, 743−745.

(10) Iijima, S.; Ichihashi, T. Single-Shell Carbon Nanotubes of 1-nm Diameter. *Nature* **1993**, *363*, 603−605.

(11) Bethune, D. S.; Kiang, C. H.; de Vries, M. S.; Gorman, G.; Savoy, R.; Vazquez, J.; Beyers, R. Cobalt-Catalyzed Growth of Carbon Nanotubes with Single-Atomic-Layer Walls. *Nature* **1993**, *363*, 605−607.

(12) Ajayan, P. M.; Lambert, J. M.; Bernier, P.; Barbedette, L.; Colliex, C.; Planeix, J. M. Growth Morphologies During Cobalt-Catalyzed Single-Shell Carbon Nanotube Synthesis. *Chem. Phys. Lett.* **1993**, *215*, 509−517.

(13) Guo, T.; Nikolaev, P.; Thess, A.; Colbert, D. T.; Smalley, R. E. Catalytic Growth of Single-Walled Nanotubes by Laser Vaporization. *Chem. Phys. Lett.* **1995**, *243*, 49−54.

(14) *Physical Properties of Carbon Nanotubes*; Saito, R., Dresselhaus, G., Dresselhaus, M., Eds.; Imperial College Press: London, 1998.

(15) Ajayan, P. M.; Iijima, S. Capillarity-Induced Filling of Carbon Nanotubes. *Nature* **1993**, *361*, 333−334.

(16) Ajayan, P. M.; Stephan, O.; Redlich, P.; Colliex, C. Carbon Nanotubes as Removable Templates for Metal Oxide Nanocomposites and Nanostructures. *Nature* **1995**, *375*, 564−567.

(17) Sloan, J.; Wright, D. M.; Woo, H. G.; Bailey, S.; Brown, G.; York, A. P. E.; Coleman, K. S.; Hutchison, J. L.; Green, M. L. H. Capillarity and Silver Nanowire Formation Observed in Single Walled Carbon Nanotubes *J. Chem. Soc.*, *Chem. Commun.* **1999**, 699−700.

(18) Ebbesen, T. W. Wetting, Filling and Decorating Carbon Nanotubes. *J. Phys. Chem. Solids* **1996**, *57*, 951−955.

(19) Sloan, J.; Novotny, M. C.; Bailey, S. R.; Brown, G.; Xu, C.; Williams, V. C.; Friedrichs, S.; Flahaut, E.; Callendar, R. L.; York, A. P. E.; Coleman, K. S.; Green, M. L. H.; Dunin-Borkowski, R. E.; Hutchison, J. L. Two Layer 4:4 Co-ordinated KI Crystals Grown Within Single Walled Carbon Nanotubes. *Chem. Phys. Lett.* **2000**, *329*, 61−65.

(20) Meyer, R. R.; Sloan, J.; Dunin-Borkowski, R. E.; Kirkland, A. I.; Novotny, M. C.; Bailey, S. R.; Hutchison, J. L.; Green, M. L. H. Discrete Atom Imaging of One-Dimensional Crystals Formed within Single Walled Carbon Nanotubes. *Science* **2000**, *289*, 1324−1326.

(21) Kirkland, A. I.; Saxton, W. O.; Meyer, R. R. Indirect Super Resolved Microscopy—Aberration Compensation and Image Reconstruction of Tilt Azimuth Data. In *The Electron. Proceedings of the International Centennial Symposium on the Electron*; Kirkland, A. I., Brown, P. D., Eds.; Institute of Materials: London, 1998; pp 426−436.

(22) Kirkland, A. I.; Saxton, W. O.; Chand, G. Multiple Beam Tilt Microscopy for Super Resolved Imaging. *J. Electron Microsc.* **1997**, *1*, 11−22.

(23) Hutchison, J. L.; Doole, R. C.; Dunin-Borkowski, R. E.; Sloan, J.; Green, M. L. H. The Development and Assessment of a High Performance Field Emission Gun Analytical HREM for Materials Science Applications. *JEOL News* **1999**, *34E*, 10−15.

(24) Phillip, F.; Hoschen, R.; Mobus, G.; Osaki, M.; Ruhle, M. The Stuttgart Atomic Resolution High Voltage Electron Microscope: Approaching 1A Point-to-Point Resolution. *JEOL News* **1994**, *31E*, 2−11.

(25) Smith, D. J. The Realisation of Atomic Resolution with the Electron microscope. *Rep. Prog. Phys.* **1997**, *60*, 1513−1580.

(26) *Electron Energy Loss Spectroscopy in the Electron Microscope*; Egerton, R. F., Ed.; Plenum Publishing: NewYork, 1996.

(27) *Transmission Electron Microscopy. 4. Spectrometry*; Williams, D. B., Carter, C. B., Eds.; Plenum Publishing: NewYork, 1996.

(28) Schiske, P. Image Processing Using Additional Statistical Information About the Object. In *Image processing and Computer-Aided Design in Electron Optics*; Hawkes, P. W., Ed.; Academic Press: London, 1973; pp 82−90.

(29) Kirkland, E. J. Improved High-Resolution Image Processing of Bright Field Electron Micrographs. *Ultramicroscopy* **1984**, *15*, 151−172.

(30) van Dyck, D.; Op de Beeck, M. New Direct Methods for Phase and Structure Retrieval by HREM. In *Proceedings of the XIIth International Congress on EM*, Seattle, 1990; pp 26−27.

(31) Coene, W.; Janssen, G.; Op de Beeck, M.; van Dyck, D. Phase Retrieval Through Focus Variation for Ultra-Resolution in Field-Emission Transmission Electron Microscopy. *Phys. Rev. Lett.* **1992**, *69*, 3743−3746.

(32) Lichte, H. Electron Image Plane Off-Axis Holography of Atomic Structures. In *Advances in Optical and Electron Microscopy*; Academic Press: London, 1991; Vol. 12, pp 25−91.

(33) Orchowski, M.; Rau, W. D.; Lichte, H. Electron Holography Surmounts Resolution Limit of Electron Microscopy. *Phys. Rev. Lett.* **1995**, *74*, 399−402.

(34) Saxton, W. O. Accurate Atom Positions from Focal and Tilted Beam Series of High-Resolution Electron Micrographs. In *Image and Signal processing in Electron Microscopy*; Hawkes, P. W., Ottensmeyer, F. P., Saxton, W. O., Rosenfeld, A., Eds.; Proceedings of the 6th Pfefferkorn Conference, Niagara, 1987; Scanning Microscopy International: Chicago, 1988; pp 213−224.

(35) Kirkland, A. I.; Saxton, W. O.; Chau, K.-L.; Tsuno, K.; Kawasaki, M. Super-resolution by aperture synthesis: tilt series reconstruction in CTEM. *Ultramicroscopy* **1995**, *57*, 355−74.

(36) Honda, T.; Tomita, T.; Kaneyama, T.; Ishida, Y. Field-Emission Ultrahigh-Resolution Analytical Electron-Microscope. *Ultramicroscopy* **1994**, *54*, 132−144.

(37) Otten, M. T.; Coene, W. M. J. High-Resolution Imaging On a Field-Emission TEM. *Ultramicroscopy* **1993**, *48*, 77−91.

(38) Krivanek, O. L.; Gubbens, A. J.; Dellby, N.; Meyer, C. E. Design and First Applications of a Post-column Imaging Filter. *Microsc. Microanal. Microstruct.* **1992**, *3*, 187−199.

(39) Tanada, M.; Tsuda, K.; Terauchi, M.; Tsuno, K.; Kaneyama, T.; Honda, T.; Ishida, M. A new 200 kV Omega-Filter Electron Microscope. *J. Microsc.* **1999**, *194*, 219−227.

(40) Meyer, R. R.; Kirkland, A. I. Characterisation of the Signal and Noise Transfer of CCD Cameras for Electron Detection. *Microsc. Res. Tech.* **2000**, *49*, 269−280.

(41) Meyer, R. R.; Kirkland, A. I. The Effects of Electron and Photon Scattering on Signal and Noise Transfer Properties of Scintillators in CCD Cameras Used for Electron Detection. *Ultramicroscopy* **1998**, *75*, 23−33.

(42) Meyer, R. R.; Kirkland, A. I.; Saxton, W. O. A New Method for the Determination of the Wave Aberration Function for High-Resolution TEM: 1. The Symmetric Aberrations. *Ultramicroscopy* **2002**, *92*, 89−109.

(43) *Structural Inorganic Chemistry*; Wells, A. F., Ed.; Oxford University Press: Oxford, 1990; p 409.

(44) Sloan, J.; Brown, G.; Bailey, S. R.; Coleman, K. S.; Flahaut, E.; Friedrichs, S.; Xu, C.; Green, M. L. H.; Dunin-Borkowski, R. E.; Hutchison, J. L.; Kirkland, A. I. The Crystallography of Metal Halides Formed Within Single Walled Carbon Nanotubes. *Proceedings of the Fall 2000 Meeting of the Materials Research Society*; MRS: Warrendale, PA, 2000; A14.3, 1−6.

(45) Sloan, J.; Friedrichs, S.; Meyer, R. R.; Kirkland, A. I.; Hutchison, J. L.; Green, M. L. H. Structural Changes Induced in Nanocrystals to Binary Compounds Confined Within Single Wall Carbon Nanotubes: a Brief Review. *Inorg. Chim. Acta* **2002**, *330*, 1−12.

(46) Sloan, J.; Kirkland, A. I.; Hutchison, J. L.; Green, M. L. H. Integral Atomic Layer Architectures of 1D Crystals Inserted Into Single Walled Carbon Nanotubes. *Chem. Commun.* **2002**, 1319−1332.

(47) Wilson, M.; Madden, P. A. Growth of Ionic Crystals in Carbon Nanotubes. *J. Am. Chem. Soc.* **2001**, *123*, 2101−2102.

(48) Friedrichs, S.; Sloan, J.; Green, M. L. H.; Hutchison, J. L.; Meyer, R. R.; Kirkland, A. I. Simultaneous Determination of Inclusion Crystallography and Nanotube Conformation for a Sb_2O_3/Single Walled Nanotube Composite. *Phys. Rev. B* **200**1, *64*, 045406/1−8.

(49) Svensson, C. Crystal Structure of Orthorhombic Antimony Trioxide. *Acta Crystallogr.* **1974**, *B30*, 458−461.

(50) Svensson, C. Refinement of the Crystal Structure of Cubic Antimony Trioxide, Sb_2O_3. *Acta Crystallogr.* **1975**, *B31*, 2016−2018.

(51) Hirahara, K.; Bando, S.; Suenaga, K.; Kato, H.; Okazaki, T.; Shinohara, H.; Iijima, S. Electron Diffraction Study of One-Dimensional Crystals of Fullerenes. *Phys. Rev. B* **2001**, *64*, 115420/1−5.

(52) Sloan, J.; Green, M. L. H. Synthesis and Characterisation of Materials Incorporated Within Carbon Nanotubes. In *Fullerenes: Chemistry, Physics and Technology*; Kadish, K. M., Ruoff, R. S., Eds.; Wiley-Interscience: New York, 2000; pp 795−838.

(53) Xu, C.; Sloan, J.; Brown, G.; Bailey, S. R.; Williams, V. C.; Friedrichs, S.; Coleman, K. S.; Flahaut, E.; Hutchison, J. L.; Dunin-Borkowski, R. E.; Green, M. L. H. 1D Lanthanide Halides Inserted into Single Walled Carbon Nanotubes. *J. Chem. Soc., Chem. Commun.* **2000**, 2427−2428.

(54) Krebs, B. Crystal Structure of Zirconium(IV) Chloride: a New AB_4-Type Structure. *Angew. Chem., Int. Ed. Engl.* **1969**, *8*, 146−147.

(55) Brown, G.; Bailey, S. R.; Sloan, J.; Xu, C.; Friedrichs, S.; Flahaut, E.; Coleman, K. S.; Green, M. L. H.; Hutchison, J. L.; Dunin-Borkowski, R. E. Electron Beam Induced *In Situ* Clusterisation of 1D $ZrCl_4$ Chains Formed Inside Single Walled Carbon Nanotubes. *J. Chem. Soc.*, *Chem. Commun.* **2001**, 845−846.

AR010169X